New Type of Inverse Opals: Titania With Skeleton Structure

Wenting Dong, Hans J. Bongard, and Frank Marlow*

Max-Planck-Institut für Kohlenforschung, Kaiser-Wilhelm-Platz 1, 45470 Mülheim an der Ruhr, Germany

Received August 26, 2002. Revised Manuscript Received November 11, 2002

A skeleton structure, consisting of titania cylinders connecting the tetrahedral and octahedral voids among the close-packed spheres of an opal template, was prepared by using an intra-template condensation process of titania among close-packed monodispersed polystyrene particles with a size of 270 nm. Theoretical calculations show that this kind of structure can exhibit a novel band gap in a lower frequency range than known inverse opals and even two complete band gaps. The realization of the titania skeleton is regarded as the first step toward a qualitative band structure tuning for inverse opals.

Introduction

Photonic crystals (i.e., spatially periodic structures of dielectric materials with different refractive indices) have been extensively investigated worldwide in the last 10 years after the pioneering works of Yablonovitch and John in 1987.[1−3] Because the lattice constant of photonic crystals is in the visible or infrared wavelength range, they can control the propagation of photons in a way similar to the way a semiconductor does for electrons. Many studies have been carried out to predict and produce the 3D complete photonic band gap structures because of their wide potential applications in optics.[1] For example, diamond lattices,[4,5] inverse opals,[6−8] cubic lattices,[9] and tetragonal lattices,[10] etc., have been proposed.

However, except inverse opals, all other structures are very difficult to be realized with a gap in the visible wavelength range. Inverse opals can be produced relatively easily in a wide range of lengths via self-assembling of monodispersed particles, which are used as a mold for the inverse structure.[11,12] It was theoretically predicted that there is a complete band gap between the 8th and 9th bands in the inverse opals.[6−8] Up to now, two kinds of inverse opal structures have been reported: the first one is a shell structure (ShS) consisting of dielectric spherical shells around air spheres, which can be produced by incomplete filling of the opal by dielectric materials;[13] the second structure is generated if the whole space among the opal spheres is filled. The second structure can be called a residual volume structure (RVS).[14]

In this paper we report another inverse opal structure with incomplete filling of the opal mold. It consists of dielectric cylinders connecting the tetrahedral and octahedral voids among the close-packed template spheres. This structure, called skeleton structure, has been shown in a short letter[15] and here we describe the full details. It can be fabricated by titania using an opal mold produced via self-assembly of monodispersed PS particles with a size of 270 nm. Similar rodlike structures of zirconia[16] and iron[17] were also observed by Holland and Yan, respectively. However, they gave only very short remarks to mention this point more or less as a peculiarity. In this paper, theoretical band structure calculations were carried out to explore the photonic properties of this inverse opal structure.

Experimental Section

Titania inverse opals were prepared by a method using polystyrene (PS) opals as a template.[11,12,18] All chemicals were used as received. First, a PS opal was made by slow drying of an aqueous suspension of PS particles (Microparticles; particle diameter 270 nm). Then pieces of 1−3 mm^3 of the PS opal were infiltrated with an excess of precursor solution of titania, i.e., mixture of titanium iso-propoxide ($Ti(i\text{-}OPr)_4$, Aldrich) and ethanol (Merck) under argon. After infiltration, the completely filled opal was separated from the precursor solution and exposed to air. In this process, the titania precursor reacts with the moisture of air. Here, we used only a one-cycle process for

* Corresponding author. Fax: 49-208-3062995. Tel: 49-208-3062407. E-mail: marlow@mpi-muelheim.mpg.de.

(1) Joannopoulos, J. D.; Meade, R. D.; Winn, N. *Photonic Crystals, Molding the Flow of Light;* Princeton University Press: Princeton, NJ, 1995.
(2) Yablonovitch, E. *Phys. Rev. Lett.* **1987**, *58*, 2059.
(3) John, S. *Phys. Rev. Lett.* **1987**, *58*, 2486.
(4) Ho, K. M.; Chan, C. T.; Soukoulis, C. M. *Phys. Rev. Lett*. **1990**, *65*, 3152.
(5) Yablonovitch, E.; Gmitter, T. J. *Phys. Rev. Lett*. **1991**, *67*, 2295.
(6) Sözuer, H. S.; Haus, J. W. *Phys. Rev. B* **1992**, *45*, 139622.
(7) Busch, K.; John, S. *Phys. Rev. E* **1998**, *58*, 3896.
(8) Li, Z. Y.; Zhang, Z. Q. *Phys. Rev. B* **2000**, *62*, 1516.
(9) Sözuer, H. S.; Haus, J. W. *J. Opt. Soc. Am. B* **1993**, *10*, 296.
(10) Temelkuran, B.; Soukoulis, C. M.; Ho, K. M. *Appl. Phys. A* **1998**, *66*, 363.
(11) Holland, B. T.; Blanford, C. F.; Stein, A. *Science* **1998**, *281*, 538.
(12) Wijnhoven, J. E. G. J.; Vos, W. L. *Science* **1998**, *281*, 802.
(13) Zakhidov, A. A.; Baughman, R. H.; Iqbal, Z.; Cui, C. X.; Khayrullin, I.; Dantas, S. O.; Marti, I.; Ralchenko, V. G. *Science* **1998**, *282*, 897.
(14) Vlasov, Y. A.; Yao, N.; Norris, D. J. *Adv. Mater*. **1999**, *11*, 165.
(15) Dong, W. T.; Bongard, H.; Tesche, B.; Marlow, F. *Adv. Mater*. **2002**, *14*, 1457.
(16) Holland, B. T.; Blanford, C. F.; Do, T.; Stein, A. *Chem. Mater*. **1999**, *11*, 795.
(17) Yan, H. W.; Blanford, C. F.; Lytle, J. C.; Carter, C. B.; Smyrl, W. H.; Stein, A. *Chem. Mater*. **2001**, 13, 4314.
(18) Wijnhoven, J. E. G. J.; Bechger, L.; Vos, W. L. *Chem. Mater.* **2001**, 13, 4486.

10.1021/cm021299i CCC: $25.00
Published on Web 01/03/2003

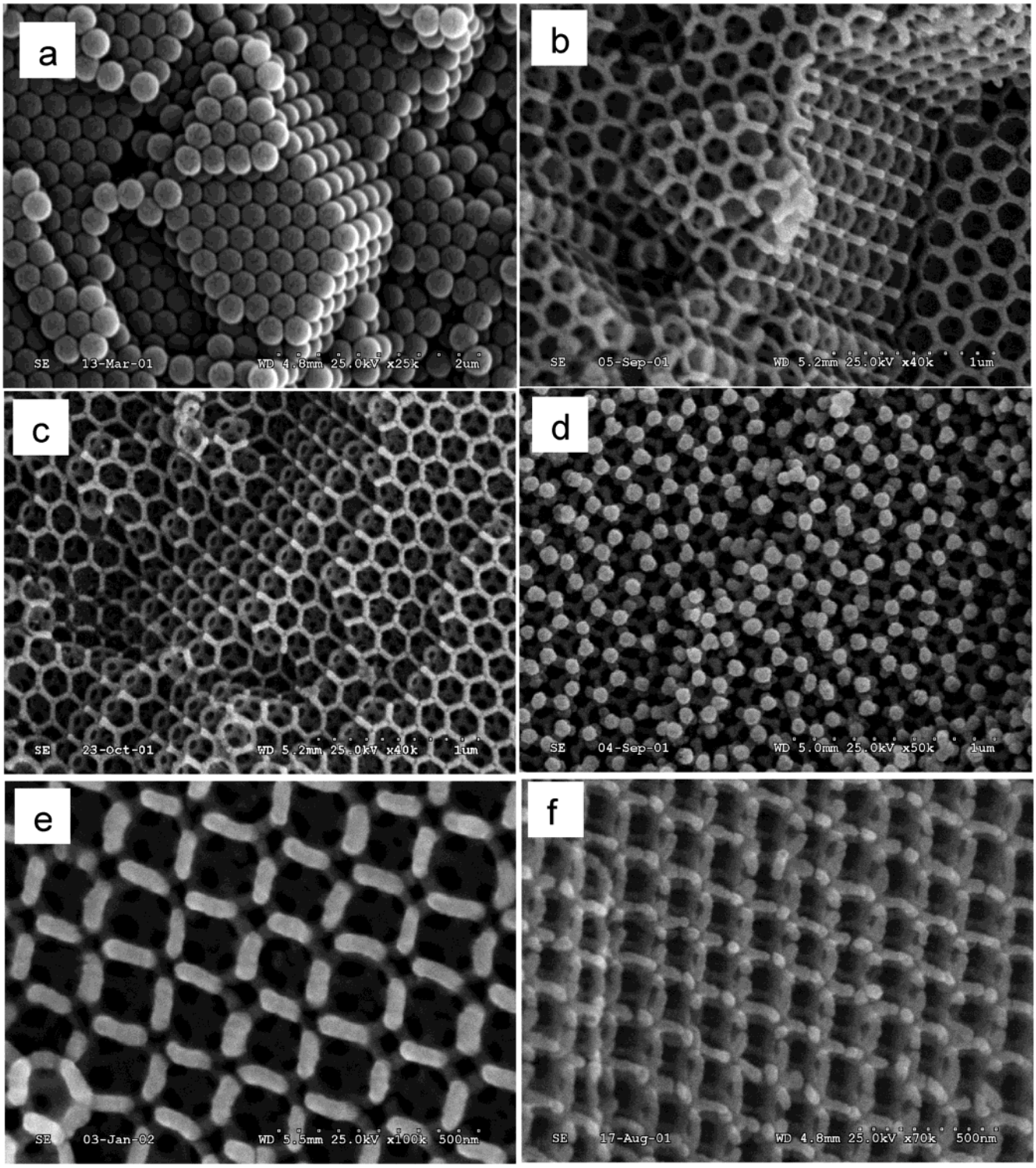

Figure 1. SEM pictures of the PS opal (a) and of skeleton structures (b−f). The pictures (b−f) depend on viewing direction and sample preparation conditions: (b) cylinder radius of $r_{cyl}/a = 0.09$; (c) cylinder radius of $r_{cyl}/a = 0.06$; (d) top-view on dangling bonds of a (111) surface; (e) top view on a (100) surface with 4-fold symmetry, and (f) tilted view on a (100) surface. The structures are observed at the inner part of the sample pieces. All these samples were prepared with 80 vol % of $Ti(i\text{-}OPr)_4$ in EtOH. Samples in b, c, d, e, and f were calcined at 300 °C for 8.5 h, at 450 °C for 2 h, at 580 °C for 8.5 h, at 450 °C for 8.5 h, and at 580 °C for 8.5 h, respectively.

the infiltration instead of a multi-cycle process.[12] Then the composite of PS and the dried titania precursor was calcined to remove the PS. Samples were produced under different conditions: the concentration of $Ti(i\text{-}OPr)_4$ in ethanol varied from 30 to 80 vol %, the drying time varied from 1 h to 5 days, and calcination temperatures ranged from 300 to 580 °C. Strong opalescence of the samples was observed under an optical microscope, revealing differently colored domains with sizes up to 300 × 300 μm. SEM pictures were taken using a Hitachi 3500N scanning electronic microscope.

Results and Discussion

Structural Characterization. Figure 1 shows SEM pictures of the PS opal template and different examples of the structure found in the inner part of the titania

inverse opal prepared by the high concentration of Ti(i-OPr)$_4$ in the precursor (80 vol %). It can be seen from Figure 1a that the opal structure is well ordered and forms the same *fcc* lattice as is known from many opal systems. The opal can be described by an *fcc* lattice with a lattice constant *a* and it contains tetrahedral and octahedral voids among the opal spheres, which are interconnected. It can be seen from Figure 1b−f that the inverse opal shows different structures, which differ clearly from those of the shell structures or residual volume structures found in previous works.[13,14] These structures are found in the inner part of the sample and turned out to be fully representative. None of the SEM pictures showed shells around the air spheres as have been visible in previous works. Instead, hexagon-like rings (Figure 1b and c), tetragon-like rings (Figure 1e and f) and hexagonal arrays of circular objects (Figure 1d) were found. The circular objects form 6-member rings and cannot be any of the cross-sections of a RVS or a ShS. Because the coexistence of the hexagon-like rings and the 6-member rings of circular objects (6RC) was found in the same SEM pictures (not shown), we assign the different pictures to different cross-sections of one and the same structure. Very likely such a structure must consist of cylinders, which provides a consistent explanation of the SEM pictures. From the side view, the cylinders form hexagon-like or tetragon-like arrays, and, from the top view, they form circular objects. Figure 1e shows the (100) direction cross-section and it contains the tetragonal arrays of bar-like objects around the air spheres. In Figure 1f also tetragon-like arrays are visible under a slightly tilted angle, revealing a cage-like arrangement of cylinders. Comparing Figure 1e and f, we conclude that every bar-like object in Figure 1e consists of two connected cylinders instead of one single cylinder, as it is visible in Figure 1f.

As we mentioned above, the skeleton structures were found at the inner part of the sample. At the surface of the sample, normally shell structures or residual volume structures can be seen. Figure 2 simultaneously shows the two different kinds of structures in the titania inverse opal prepared by the high concentration of Ti(i-OPr)$_4$ in the precursor (80 vol %). The first kind is a shell structure existing at the surface of the sample (inside the two marked triangles in Figure 2a), which is shown in Figure 2b with a high electron microscopic magnification. It consists of hexagonal arrays of titania shells around the air spheres with triangle-like secondary voids among three neighboring air spheres. In addition to this shell structure, another structure is found at a deeper part of the sample (inside the marked square in Figure 2a), shown with more details in Figure 2c. The structure shown in Figure 2c consists of hexagonal arrays of hexagon titania rings instead of circular titania rings around the air voids.

Many modifications of the synthesis procedure have been investigated. Although variations in the pore volume have been observed, always skeleton structures occurred in the inner part of the samples prepared with the 270-nm PS opal template while shell structure existed at the surface of the sample pieces. Therefore, the structure of the fabricated inverse opal depends not only on the preparation conditions, but also on the location in the sample.

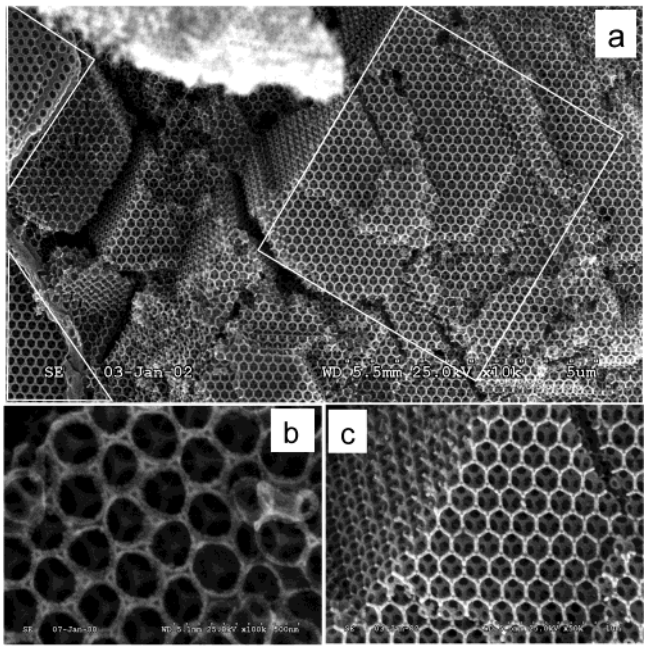

Figure 2. SEM pictures of the titania inverse opal with two kinds of structures on the view field (a). Details: (b) shell structure near the surface and (c) skeleton structure in the deeper part of the sample. The triangles and square with white lines highlight the different regions. The sample was prepared with 80 vol % of Ti(i-OPr)$_4$ in EtOH and calcined at 450 °C for 8.5 h. This sample is the same sample as that shown in Figure 1e.

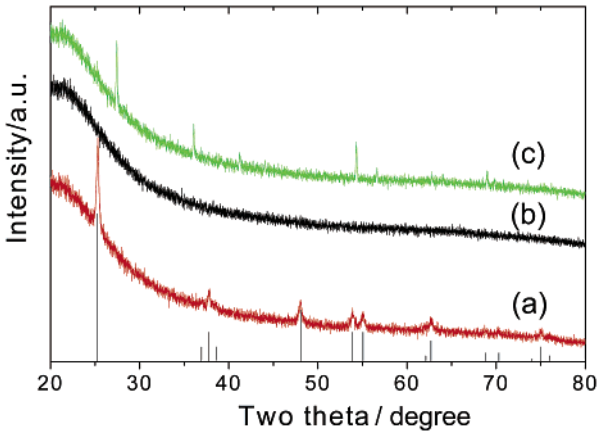

Figure 3. XRD pattern of the titania skeleton inverse opal taken in transmission mode. The diffraction pattern of the sample calcined at 580 °C (curve a) coincides with that of the bulk anatase,[19] shown as the sharp lines at the bottom of the figure. The sample for XRD measurement was prepared by mixing the titania skeleton with silicon oil between two transparent foils. The high background arises from the silicon oil (curve b). The XRD pattern of a sample calcined at 1000 °C is shown for comparison (curve c). It reveals the rutile phase of titania, but the skeleton macrostructure is mostly destroyed under these conditions.

The different behavior in the different sample regions can be assigned to the different drying and reaction conditions. The outer regions release ethanol and propanol much more efficiently and can be reached much faster by the humidity of the air. Very likely, this leads to locally fast hydrolysis and condensation reactions in the infiltrated solution resulting in quick precipitation of TiO_2 without intermediate gel formation. On the

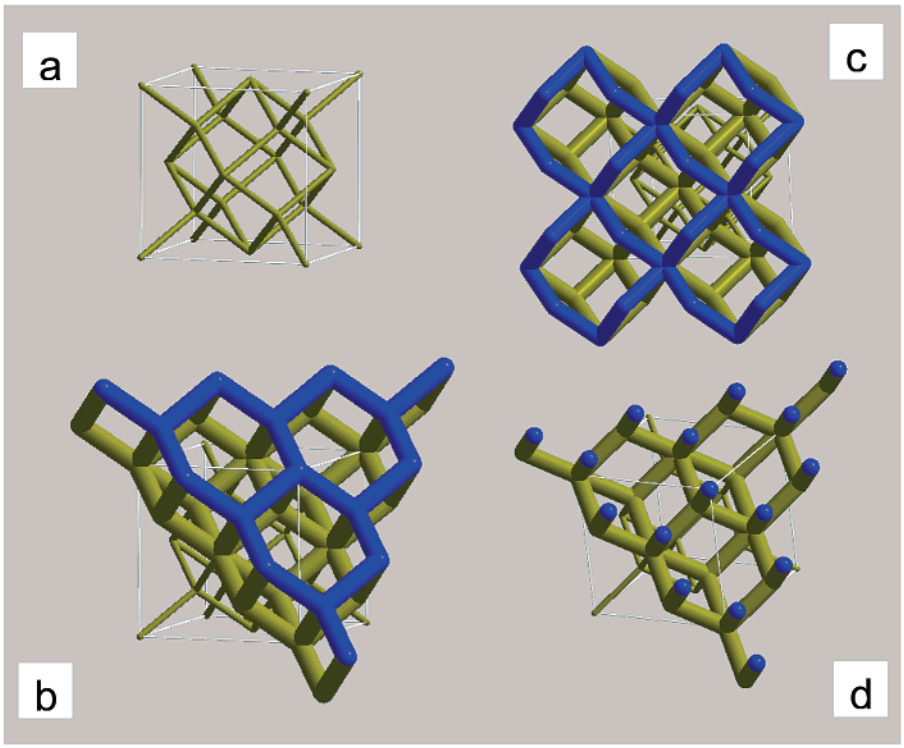

Figure 4. Model of the skeleton structure: (a) cubic unit cell with the lattice constant *a*; (b) the same unit cell with two layers of thicker cylinders to show the hexagonally ordered network of the (111) surface; (c) the same unit cell with two layers of thicker cylinders to show the tetragonally ordered squares of the (100) surface; (d) (111) surface with dangling bonds forming a hexagonal array of 6-member rings of circular bond endings (6RC).

contrary, in the internal parts of the material the reaction is slower. Therefore, a gel can be formed in an intermediate step, which might shrink more seriously than the material at the sample surface during the following drying and condensation process. This leads to the cylinder-like structure parts driven by surface energy lowering. Because the synthesis is strongly connected with diffusion processes, inhomogeneity of the sample is very likely, leading to the coexistence of the ShS and the skeleton structure. Inhomogeneous phenomena in such condensation process have also been observed by other researchers.[16]

Concerning the skeleton structure there is another interesting fact worth noting. The relative radius of a cylinder (r_{cyl}/a) fitting among 3 close-packed template spheres must be smaller than 0.055. However, the relative cylinder radii found for our samples are in the range of 0.06−0.1, which are larger than 0.055. For example, the realized relative cylinder radii of the skeleton structures shown in Figure 1b and c are about 0.09 and 0.06, respectively. The cylinder radius seems to exceed the maximum cylinder radius among three spheres of the opal template. This means that the skeleton structure is not only a partial filling of the residual empty space of the original opal. We assign this more complicated structure formation to the calcination process, during which three important effects occur simultaneously: combustion of the template sphere, condensation and growth of the infiltrated material, and obviously, a redistribution of the infiltrated material. Two important parameters have been proven to be decisive in the preparation process: concentration of the precursor and calcination temperature. It has been found that higher concentrations and lower calcination temperatures lead to larger cylinder radius.

The cylinders in the skeleton structure have been found to consist of the anatase phase of titana. Figure 3 shows the XRD pattern of the titania inverse opal calcined at 580 °C. The position of the diffraction peaks coincides very well with the standard value of the bulk anatase phase of titania.[19] We note that the diffraction peaks are slightly broadened, which indicates that the titania cylinders consist of small titania particles. Therefore, the titania cylinders are very likely porous and the refractive index of titania skeleton is somewhat less than 2.5, which is the refractive index of anatase. The porosity characterization is under progress right now.

Model of the Skeleton Structure. On the basis of the SEM pictures of the skeleton structure, a model of the structure has been constructed. On one hand this model should provide a consistent description of the SEM pictures, and on the other hand it enables the prediction of the photonic properties of the skeleton structure. Let us consider an *fcc* lattice of close-packed template spheres. Among the spheres there are interconnected tetrahedral and octahedral voids. If we connect the tetrahedral and octahedral centers of the voids by cylinders, then we can get a skeleton model structure, as shown in Figure 4. Each cage (see Figure 4a) which replaces the former template sphere is surrounded by another 12 cages with one cylinder lying among every 3 neighboring cages. Every cage is a rhombododecahedron, which is composed of 24 cylinder-like edges. The cubic unit cell shown in Figure 4a contains 8 tetrahedral and 4 octahedral sites (refers to the tetrahedral and octahedral sites in the opal template mentioned above), which form a calcium fluoride structure with the space group *Fm-3m*. Here the bonds between Ca^{2+} and F^- are

(19) ICDD Database, STOE & Cie GmbH, **1999**; Card no. 21-1272.

replaced by the cylinders of the skeleton structure. It is possible to use 8 different cylinders to generate the whole skeleton structure. The coordinates of the centers of 8 cylinders are (±0.125a, ±0.125a, ±0.125a), if we put an octahedral center in the origin. The cylinder length is $\sqrt{3}a/4$.

Figure 4b and c show a larger region of the structure with two layers of cylinders with enlarged radius which could form a surface. Such a surface might be visible in SEM. In Figure 4b, all the dangling bonds are removed and the surface is formed by a closed network. In Figure 4c, one example of remaining bond loops are shown with (100) as the front face, which can also be seen from Figure 1e and f. A surface with dangling bonds in the (111) direction is shown in Figure 4d. This can result in the 6RC pictures in SEM (see Figure 1d). It is very likely that different structures are realized during breaking of the sample. The SEM pictures found are very similar to those models.

Band Structure Calculations. It is very important to find out if the new skeleton structure has photonic band gaps. Therefore, band structure calculations were carried out using the mpb program, which was developed by the Joannopolous group at MIT.[20] This program can find the fully vectorial eigen modes of Maxwell equations in periodic lattices using a plane wave basis.[21]

Figure 5a and b show the band structures of skeleton with relative cylinder radii of 0.074 and 0.096, respectively (with a dielectric constant of the cylinders of 11.9, which is that of silicon) and Figure 5c shows the band structure of a silicon RVS with relative air sphere radius of 0.35355. Comparing the band structure of the skeleton with those of the shell structure or RVS, it can be seen that all can have a gap between the 8th and 9th bands, but the pseudo-gap between the 5th and 6th bands for the RVS is completely opened for the skeleton structure. This band gap between the 5th and the 6th bands (abbreviated as 5−6 gap) has never occurred for the RVS or ShS. This novel gap can occur alone or together with the expected gap between the 8th and 9th bands (abbreviated as 8−9 gap).

The 5−6 gap of the skeleton structure lies between the lower energy band edge at the center of the Brillouin zone (Γ point) and the upper band edge at 12 symmetry-equivalent points, which are lying between the Γ and K points (at about 0.082 k(K)). The 8−9 gap of the skeleton structure, shown in Figure 5b, is between the lower band edge at Γ point and the upper band edge at W point. However, for the RVS, the 8−9 gap is between the lower band edge at W point and the upper band edge at X point. Therefore, the properties of the 8−9 gap for the skeleton structure and RVS are not exactly the same.

The maximum gap sizes for the 5−6 gap and the 8−9 gap are found to be 8.9% and 3.2% of the gap center-frequency for a silicon skeleton with optimized relative cylinder radii of 0.074 and 0.096, respectively (used grid size for calculation: 32). These values depend slightly on the numerical parameters. The gap size for 5−6 gap is larger than that of 8−9 gap in the optimized skeleton structure. Moreover, the gap size for 5−6 gap is also larger than that of the 8−9 gap in the RVS, which is 4.9% if it is calculated with the same accuracy (radius of air spheres: 0.35355). The simultaneous existence of the two gaps can also be achieved for different radius of cylinders. This coexistence of the two low-frequency gaps is new for practically accessible systems and may have interesting optical applications.

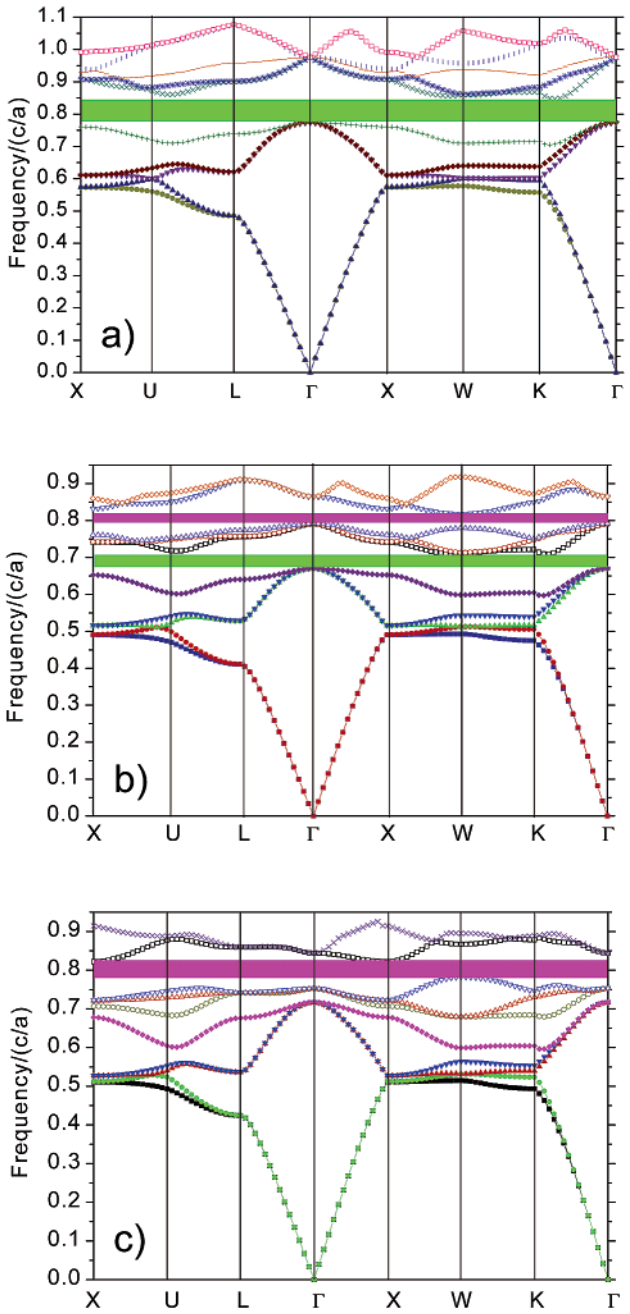

Figure 5. Photonic band structures optimized to show a maximum band gap (a) between 5th and 6th bands (r_{cyl}/a = 0.074) and (b) between the 8th and 9th bands (r_{cyl}/a = 0.096), respectively. The latter structure is also an example for the simultaneous occurrence of two low-energy band gaps. The traditional way of showing band structures has been completed by adding one more line of k-points of the Brillouin zone to show all relevant band extrema. (c) The band structure for the RVS is given for comparison (r_{air}/a = 0.35355). Parameters used for the calculation: epsilon, 11.9; grid size, 32; mesh size, 7.

(20) Johnson, S. G.; Joannopoulos, J. D. *The MIT Photonic-Bands Package*; http://ab-initio.Mit.edu/mpb/.
(21) Johnson, S. G.; Joannopoulos, J. D. *Optics Express* **2001**, *8*, 173.

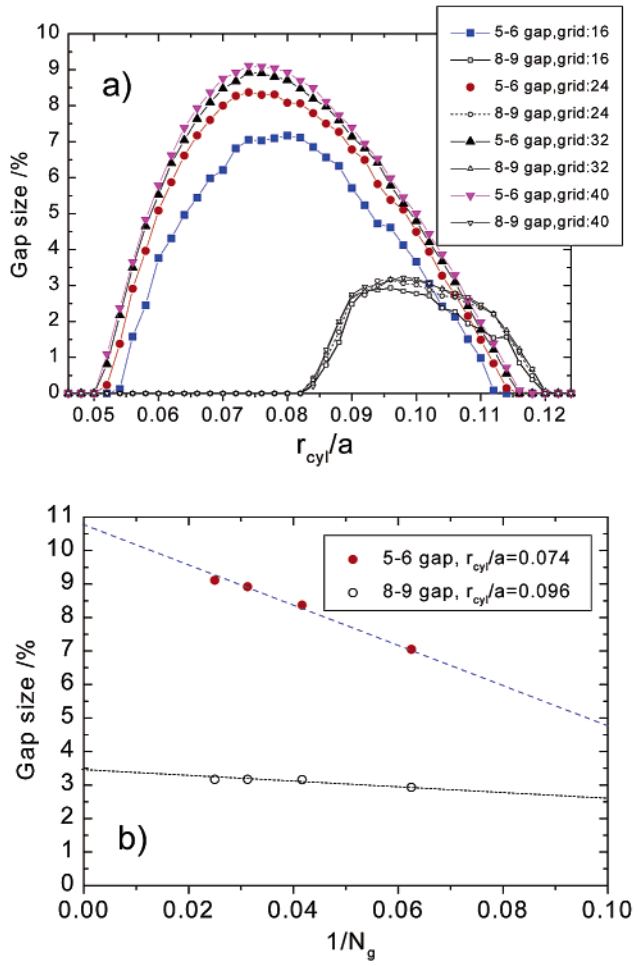

Figure 6. (a) Dependence of the gap size on the radius of cylinder in the skeleton structure. The influence of the grid size on the radius range is shown by four curves calculated with different grid sizes. (b) Dependence of the gap size on the grid size. The maximum gap sizes of about 10.7% and 3.5% for the 5−6 gap and the 8−9 gap, respectively, are obtained by extrapolation of the grid size N_g to infinity. Other parameters used for calculation are the same as those in Figure 5.

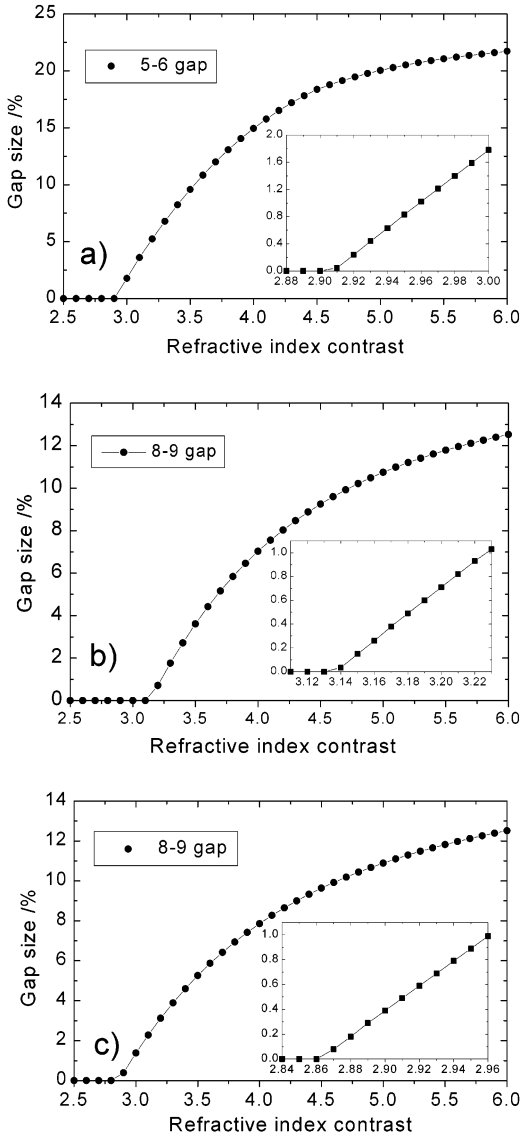

Figure 7. Dependence of the gap size on the refractive index contrast for the skeleton structure: (a) gap between 5th and 6th bands ($r_{cyl}/a = 0.074$); and (b) gap between the 8th and 9th bands ($r_{cyl}/a = 0.096$). Curve (c) gives this dependence for the gap between the 8th and 9th bands of RVS ($r_{air}/a = 0.35355$). The insets show these dependences in narrowed refractive index ranges. In the narrowed refractive index range, the dependence of gap size on refractive index is linear above the critical refractive index constant. This can be used for a more exact determination of the critical refractive index, resulting in 2.91, 3.14, and 2.86 for (a), (b), and (c), respectively. Other parameters used for calculation are the same as those in Figure 5.

The radius range for the existence of the gaps is important to investigate because it shows the stability of the gaps against structure parameter variations. Figure 6 shows the relationship between gap size and radius of the cylinders for a skeleton structure with a refractive index contrast of 3.45. The dependence is also slightly influenced by the accuracy of the calculations, i.e., by the grid size used for discretization. It can be seen from Figure 6a that the accuracy of the calculation influences the radius range for the appearance of the gaps as well as the maximum gap width. For the 5−6 gap, the influence of the grid size on radius range is larger than that of the 8−9 gap. As the grid size increases from 16 to 40, the radius range for 5−6 gap increases first and then it seems to become constant. For the highest accuracy used, the 5−6 gap opens in the radius range of $0.05 < r_{cyl}/a < 0.116$. However, the 8−9 gap is not so sensitive to the changes of grid size and it comes up always in the radius range of $0.082 < r_{cyl}/a < 0.120$ regardless of the grid size. Simultaneous band gaps occur in the radius range of $0.082 < r_{cyl}/a < 0.116$. According to these curves, one can estimate the construction possibilities of the band gaps by skeleton structures. As we noted before, titania cylinder radii between 0.06 and 0.1 have been realized by the used preparation conditions. Therefore, materials with the 5−6 gap can be achieved, and also materials with two band gaps are realistic.

Corresponding to the radius range, the filling ratio range can be calculated. The filling ratio describing the volume percentage of the high-refractive-index material in the whole photonic crystal is suited to comparing the properties of different kinds of photonic crystals. Ranges of 9.4−40.2% and 22.7−42.4% have been found for the existence of 5−6 gap and 8−9 gap, respectively. The filling ratio range for the existence of at least one gap

is 9.4−42.4%, which is larger than the filling ratio range for the occurrence of a band gap in the RVS, which is 14.2−37.7% (corresponding to the radius range for the air spheres of 0.334−0.375). Therefore, there is a broader filling ratio range usable for the skeleton structure than that of the RVS, which means a higher stability of the gap for the skeleton structure than that of the RVS against structure parameter variations.

As mentioned before, the gap sizes depend slightly on the used numerical parameters. This dependence is shown in Figure 6b. It reveals that the influence of the grid size on the gap size of 5−6 gap is larger than that of the 8−9 gap. If the grid size is extrapolated to an infinite number, the maximum gap sizes for 5−6 gap and 8−9 gap are about 10.7% and 3.5%, respectively, for a silicon skeleton structure.

The critical refractive index is very important for the fabrication of the skeleton structure with complete photonic band gaps. The dependence of the gap size on the refractive index of the skeleton material is shown in Figure 7a and b. These panels display a critical refractive index of 2.9 for the appearance of the 5−6 gap and of 3.1 for the 8−9 gap. The insets in Figure 7a and b show this dependence in a more narrow refractive index range. It is worth noting that the lowest found critical refractive index for the 5−6 gap is very close to that of the 8−9 gap for the RVS structure, as indicated in Figure 7c. The reason behind this result is still unknown.

For titania skeleton structure, only pseudo gaps can be observed because the titania skeleton does not have a high enough refractive index (it is less than 2.5). Complete photonic band gaps are expected for other higher refractive index materials, i.e., silicon and germania with refractive indexes of 3.45 and 3.92,[22] respectively, in the IR wavelength range, and GaP and CdTe with refractive indexes of 3.32 and 3.21, respectively,[22] in the visible wavelength range.

Conclusions

A new kind of inverse opals with skeleton structure was achieved by incomplete filling of a PS opal by titania obtained via a transformation process from a titania precursor. It consists of dielectric cylinders connecting the tetrahedral and octahedral centers among the close-packed air spheres with an *fcc* lattice. The materials with skeleton structure are photonic crystals with two possible complete photonic band gaps: the 5−6 gap and the 8−9 gap. The filling ratio range for the existence of at least one gap for the skeleton structure is larger than that of the RVS. The critical refractive index for the existence of 5−6 gap for the skeleton structure and 8−9 gap for the RVS are very similar, i.e., about 2.9. The skeleton structure can even have two complete band gaps occur simultaneously, making it very interesting for further investigation.

Acknowledgment. We thank F. Schüth for encouragement and support of this work and H. Lenk for his help in the numerical calculations. Support by the Fonds der Chemischen Industrie is also gratefully acknowledged.

CM021299I

(22) Yoffe, A. D. *Adv. Phys.* **1993**, *42*, 173.